
Article:
Silva, SC, Silva, AB, Folena, MC et al. (3 more authors) (2020) Cracking mechanism in API 5L X65 steel in a CO2-saturated environment – Part II: A study under cathodic polarisation. Engineering Failure Analysis, 113. 104550. ISSN 1350-6307

https://doi.org/10.1016/j.engfailanal.2020.104550

Cracking mechanism in API 5L X65 steel in a CO_2-saturated environment – Part II: A study under cathodic polarisation

S.C. Silva[1], A.B. Silva[1], M.C. Folena[1], R. Barker[2], A. Neville[2], J. A. C. Ponciano Gomes*[1]

[1]Federal University of Rio de Janeiro, Department of Metallurgical and Materials Engineering, Labcorr, Rio de Janeiro, Brazil

[2]Institute of Functional Surfaces, Faculty of Mechanical Engineering, University of Leeds, Leeds, United Kingdom, LS2 9JT

ABSTRACT

The aim of this work is to achieve a better understanding of hydrogen effect in CO_2 environments, isolating its contribution by imposing cathodic polarisation on Hydrogen Permeation (HP) and Slow Strain Rate Tests (SSRTs). The influence of Fe_3C and $FeCO_3$ layers on hydrogen embrittlement (HE) susceptibility was a specific focus of this study. The results indicate that CO_2 environment generates hydrogen, which permeates through steel, although in lower amount compared to H_2S environments. Moreover, in Fe_3C-rich surface, the HP current achieves values higher than in wet-ground surface. Furthermore, in $FeCO_3$-filmed surface HP current is higher at the beginning of the test but decreases over time. The results of SSRT show the loss of ductility of the steel under cathodic polarisation that was driven by hydrogen and the embrittlement effect magnitude depends on the surface condition, indicating that a pre-corroded steel surface can raise the HE susceptibility in a CO_2 environment.

Key words: hydrogen embrittlement, cathodic polarisation, CO_2 corrosion, surface layers, pipeline steel failures.

1. INTRODUCTION

Carbon steel pipelines are widely used due to their high yield strength while maintaining enough ductility as required by structural materials [1]. Pipeline steels must have high strength and fracture toughness as well as provide an economical and safe option to transport oil and natural gas along far distances [2-4]. However, carbon steels are susceptible to uniform corrosion in aqueous environments [1] being CO_2 corrosion one of the major integrity issues for the oil and gas industry. Also known as “sweet corrosion”, this particular degradation mechanism has been reported to cause 25% of safety

*Corresponding Author – Email address: ponciano@metalmat.ufrj.br

incidents. It has been associated with damage by both general and localised corrosion. Furthermore, the presence of corrosion products/films has been shown to have a significant effect on the corrosion mechanism [5,6]. Transgranular Stress Corrosion Cracking (TGSCC) has been studied and related to environments with CO_2 as a main contaminant [5]. Among the determining factors of TGSCC is hydrogen embrittlement. It is known that the application of a cathodic potential below the thermodynamic equilibrium potential H/H^+ ensures the hydrogen generation in metallic interface. Based on this, Asher [7] examined the effect of hydrogen on mechanical properties of pipeline steels by using slow strain rate tests. Initial tests were conducted in the standard TGSCC environment with the application of cathodic polarisation to ensure that hydrogen would be generated at the steel surface and then would permeate into the steel test specimens. Increased hydrogen generation on the steel surface by cathodic polarisation resulted in a reduction of deformation to failure, thereby indicating loss of ductility. As previously mentioned, further important aspect to be understood in CO_2 corrosion is the influence of corrosion products formed on the carbon steel surface. In CO_2-saturated aqueous environment, the formation and precipitation of iron carbonate ($FeCO_3$) and iron carbide (Fe_3C) enrichment can occur [8] and these layers can be protective or harmful for the pipeline steel.

The aim of this work is to assess the influence of surface conditions on the hydrogen permeation and hydrogen embrittlement characteristics of API 5L X65 carbon steel in a CO_2-saturated saline environment, under cathodic polarisation. This was done by comparing wet-ground surface specimens with Fe_3C-enriched and $FeCO_3$-filmed surfaces. Firstly, Fe_3C and $FeCO_3$ rich surfaces were separately obtained under adjusted conditions that propitiate formation of each specific corrosion product. Cathodic polarisation measurements were carried out in the environment of this study, CO_2-saturated 3.5 wt.% NaCl solution at room temperature, in order to evaluate the effect of the different surface layers on the cathodic reactions. Hydrogen permeation measurements were performed in this same solution under constant cathodic polarisation to determine the influence of the film on the hydrogen permeation current. Finally, Slow Strain Rate Tests (SSRTs) were conducted in order to evaluate the hydrogen effect into the tensile specimens, isolating its contribution in cracking susceptibility, according to NACE TM0198 and ASTM G129 standards [9,10]. These tests were performed in both air in order to get a baseline condition, and in saline environment using the hydrogen permeation data as a reference to adjust the loading method of the tensile specimens. Furthermore, this is a complementary work to Silva et al. [11], which studied these same surfaces conditions in the same corrosive environment

but in Open Circuit Potential, where overlap of anodic dissolution and hydrogen uptake contributions could not be avoided.

2. EXPERIMENTAL PROCEDURE

API 5L X65 carbon steel of ferritic-pearlitic microstructure was the material used in this study. Table 1 shows the chemical composition of the steel that was the same used by Silva et al. [11].

C	Si	Mn	P	S	Cr	Mo	Cu	V	Fe
0.10	0.19	1.43	0.007	0.001	0.12	0.16	0.07	0.09	Balance

Table 1: Elemental composition (wt.%) of API 5L X65 carbon steel [11].

The development of this work occurred in three steps:

I. Film generation/growth;
II. Hydrogen permeation experiments;
III. Slow strain rate tests (SSRT).

Three surface conditions were employed to subsequently perform the hydrogen permeation and SSR tests, these were: wet-ground surface; Fe_3C-rich surface and $FeCO_3$-filmed surface. The Fe_3C enrichment surface and $FeCO_3$ film generation and growth were manufactured on circular plates of steel of 25 mm diameter and 3 mm thickness for hydrogen permeation tests, and on tensile standard specimens of 3.81 mm diameter and 25.4 mm length were used for the SSRTs [11].

Fe_3C rich surface was generated in a CO_2-saturated 3.5 wt% NaCl solution at pH 3.8, at 30 °C for 20 h. Moreover, $FeCO_3$ film surface was generated in a CO_2-saturated 3.5 wt% NaCl solution at pH 6.6, at 70 °C for 20 h [11].

This work adopted the same method used by Silva et al. [11] to correlate the dissolution and/or the film formation with the evolution of corrosion rate of each specimen. For this, Linear Polarisation Resistance (LPR) technique and separate anodic and cathodic polarisation scans were performed, respectively, during and just after the tests of film formation on the steel surface. The polarisation resistance (Rp) and anodic and cathodic Tafel constants were determined from these tests and then the conversion of the charge-transfer resistance (Rct) into corrosion rate was gotten based on Stern-Geary coefficient along with Faraday's Law.

Moreover, after film formation, cathodic polarisation scans were conducted on each specimen, into the CO_2-saturated 3.5 wt.% NaCl solution, at room temperature and pH

3.8 to assess their cathodic characteristics which could be correlated with the hydrogen uptake and permeation process, as well as it was shown by Silva et al. [11].

2.1. Hydrogen Permeation Tests

Hydrogen permeation measurements were carried out using a Devanathan-Stachurski cell at room temperature. Measurements were conducted on circular plate steel with an exposed surface area of 1 cm^2 to each side of the cell. All tests were performed under a constant cathodic polarisation of 500 mV below the OCP (-500mV_{OCP}) in CO_2-saturated 3.5 wt.% NaCl brine solution, at pH 3.8 and room temperature, for 20 hours. Silva et al. [11] displayed the schematic drawing of the Devanathan-Stachurski cell.

The left compartment of the cell is the cathodic side, where CO_2 gas was continuously bubbled and in which the hydrogen generation occurs. Hydrogen generation was provided by imposing the potential of -500 mV_{OCP}, in order to isolate the hydrogen contribution in the experiment and avoid the anodic dissolution of the steel. The right compartment of the cell is the anodic side, in which the anodic potential of 100 mV_{OCP} was applied and where the oxidation of atomic hydrogen that diffuses through the specimen occurs. The anodic solution used was 1 M NaOH. Both cell compartments contained an Ag/AgCl reference electrode (RE), a platinum counter electrode (CE) and the working electrode (WE), which is the plate of steel positioned in the central part of the cell separating the anodic and cathodic compartments.

2.2. Slow Strain Rate Tests (SSRTs)

SSRTs in air were previously performed to assess the mechanical response of the steel without any influence of the environment. These results were compared to those obtained in a CO_2-saturated environment for the steel with different surface conditions under cathodic polarisation. Standard specimens were used, according to NACE TM0198 [9]. All tests were performed under controlled cathodic polarisation of -500 mV_{OCP} and under the strain rate of $4.7x10^{-6}$ s^{-1}.

SSRT conditions were similar to the used by Silva et al. [11], but under constant cathodic polarisation and the hydrogen permeation curves were also used as a reference to the loading process outset.

SSRT conditions are:

- In air
- CO_2-saturated 3.5% NaCl solution under -500mV_{OCP}:

- Wet-ground surface:
  - A1: Relative to t_0=0. This condition implies that the loading process starts when hydrogen diffusion begins on the hydrogen permeation on the wet-ground surface specimen;
  - A2: Relative to time (t_{ss}) required to achieve the hydrogen diffusion steady state. Loading of SSRT starts after hydrogen saturation of the specimen;
- Fe_3C-rich surface
  - B1: Relative to the condition similar to that defined for A1, but on the Fe_3C-rich surface specimen;
  - B2: Relative to the condition similar to that defined for A2, but on the Fe_3C-rich surface specimen;
- $FeCO_3$-filmed surface
  - C1: Relative to the condition similar to that defined for A1, but on the $FeCO_3$-filmed surface specimen;
  - C2: Relative to the condition similar to that defined for A2, but on the $FeCO_3$-filmed surface specimen;

3. RESULTS AND DISCUSSION

3.1. Surface film formation and characterisation

Similar methodology of Silva et al. [11] was used to produce different steel surface compositions and surface analysis procedures. The OCP and corresponding corrosion rate as a function of time during film formation was reported. Morphology and composition of Fe_3C-rich and of $FeCO_3$-filmed surface were defined by SEM images and XRD analysis.

During the Fe_3C-rich surface formation experiments was observed an increase of corrosion rate that was attributed to the preferential dissolution of ferrite phase, leading to a Fe_3C-rich surface [11], which increments the cathodic reaction rate, induced by either internal acidification, galvanic effects or a combination of both [12-14].

Along the $FeCO_3$ film formation Silva et al. [11] observed a corrosion rate decreasing as from a peak, associated to the surface blocking effect provided by the $FeCO_3$ crystals, which were clearly covering the majority of the steel surface area [11,15,16]. $FeCO_3$ film formed presented an average thickness of 14.58 μm.

According to Silva et al. [11], the cathodic polarisation curves of wet-ground surface presented fast cathodic reaction close to OCP, due to the reaction controlled by charge-

transfer. As from a value still close to OCP, around -40 mV_{OCP}, the shape of curve changes, showing a limiting cathodic current region, due to the mass transport. At this range of potential, the cathodic reaction is slower, this behaviour is associated with the direct reduction of H^+ and a buffering effect of carbonic acid near to the steel surface [17]. The cathodic potential selected to perform hydrogen permeation and slow strain rate tests was within the immunity domain of the thermodynamic Pourbaix diagram and consequently metal dissolution was suppressed during these experiments [18,19].

For the Fe_3C rich steel surface there was an accentuation of cathodic reaction in the diffusion-controlled potential range, which was attributed to its ability to rise the cathodic reactions and provide a lower overpotential for the hydrogen reduction reaction [13,14,20]. $FeCO_3$ film reduces significantly the cathodic reactions rate, due to a surface blocking effect from $FeCO_3$ crystals, and also as a diffusion barrier, hindering the movement of electrochemically active species [16,21].

Electrochemical driving forces for the hydrogen reduction reaction can be expressed in terms of the cathodic overpotential for the experimental conditions adopted during hydrogen permeation and SSRTs. These corresponding values are shown on Table 2. This driving force was higher for the wet-ground surface condition and lower for $FeCO_3$ precipitated surface condition.

Table 2: OCP and Cathodic potentials imposed in CO_2-saturated 3.5 wt.% NaCl solution in pH 3.8 for the different surface conditions, equilibrium potential for H^+/H_2 reduction reaction and driving force for hydrogen reduction.

	pH	OCP ($V_{Ag/AgCl}$)	Cathodic Pot. imposed ($V_{Ag/AgCl}$)	Eq. Pot. H^+/H_2 ($V_{Ag/AgCl}$)	Hydrogen Reduction Driving Force ($V_{Ag/AgCl}$)
Wet-ground surface	3.8	-0.685	-1.185	-0.432	0.753
Fe_3C		-0.665	-1.165		0.733
$FeCO_3$		-0.650	-1.150		0.718

Equilibrium potential for H^+/H_2 reduction reaction was obtained from Nernst Equation, Eq. (1), in which relates the electrode potential and the solution concentration, in order words, the solution pH. Then, the equation for the hydrogen concentration in solution is:

$$E_{(H+/H2)} = E^0_{(H+/H2)} - (0.059/n) \log[H^+] \quad \text{Eq. (1)}$$

Where,

$E^0_{(H+/H2)}$ is the standard hydrogen potential and pH = -log $[H^+]$.

Seeing that, the equilibrium potential for H^+/H_2 reduction reaction was obtained from Eq. (2):

$E_{(H+/H2)} = E^0 + (0.059/n)\ pH$ Eq. (2)

Therefore,

$E_{(H+/H2)} = 0 + (0.059/1)\ 3.8$

$E_{(H+/H2)} = 0.224\ mV_{(H+/H2)}$

The converting of potential values from standard hydrogen electrode to silver/silver chloride electrode at 25° C is 0.208 $mV_{Ag/AgCl}$. Then, the equilibrium potential for hydrogen reduction is exhibited to follow:

$E_{(H+/H2)} = 0.224 + 0.208 = 0.432\ mV_{Ag/AgCl}$

3.2. Hydrogen Permeation Tests

The effect of the different surface compositions on the hydrogen permeation current density is shown in Figure 1. The permeation curves corresponding to wet-ground samples, tests at -500 mV below OCP, presented a continuous increase of hydrogen permeation current with time. The Fe_3C-rich surface specimens presented a permeation current profile similar to the wet-ground surface but achieving higher permeation currents. Specimens with a $FeCO_3$ film on the surface presented an initial permeation current high at the beginning of the test and attenuated with time.

The continuous decrease of hydrogen permeation current density for the $FeCO_3$ filmed surface can be associated with the increasing size of the precipitated particles. The analysis of surface by SEM before and after permeation showed an increase in the $FeCO_3$ particle average size. Another effect observed at the end of the tests was the covering of pre-existing voids previously observed (Figures 2). Both phenomena, the increase of particle size and filling voids, can drive to a more effective surface barrier for hydrogen uptake and permeation. Figure 2 presents the SEM images, the image processing and the $FeCO_3$ particles analysis and count, before and after hydrogen permeation test, respectively. Table 3 displays the average particle size, percentage of covered area by the film and the number of particles of $FeCO_3$ counted by area, before and after hydrogen permeation test. The Figure 2 and Table 3 support the conclusion that $FeCO_3$ particles expand during the hydrogen permeation test under cathodic condition and cover the pre-existing voids on the film.

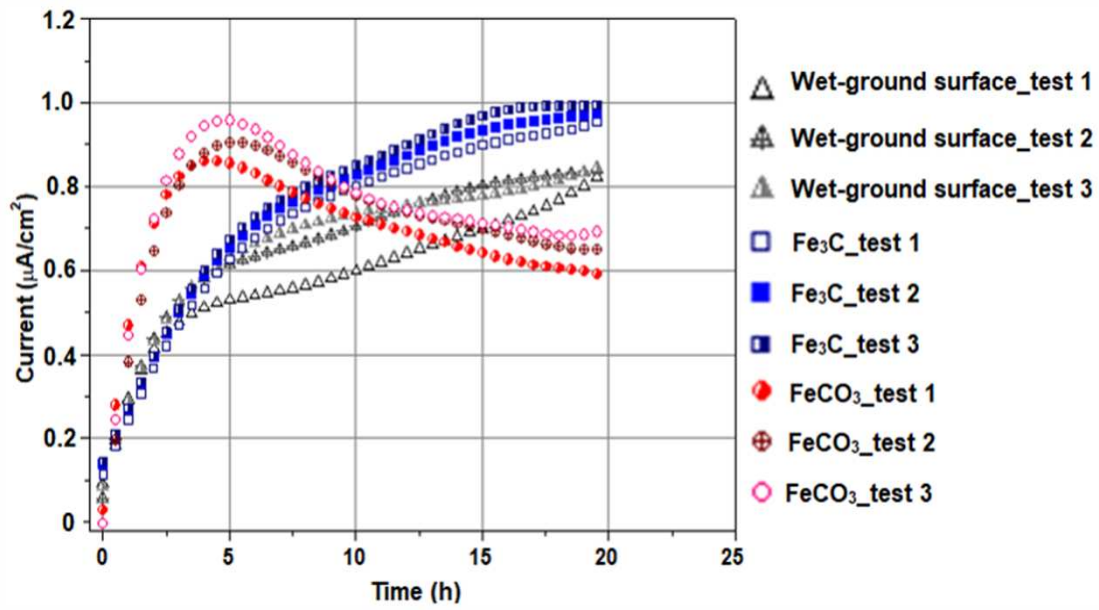

Figure 1: Hydrogen permeation curves for all surface conditions, at controlled cathodic potential of 500 $mV_{Ag/AgCl}$ below OCP.

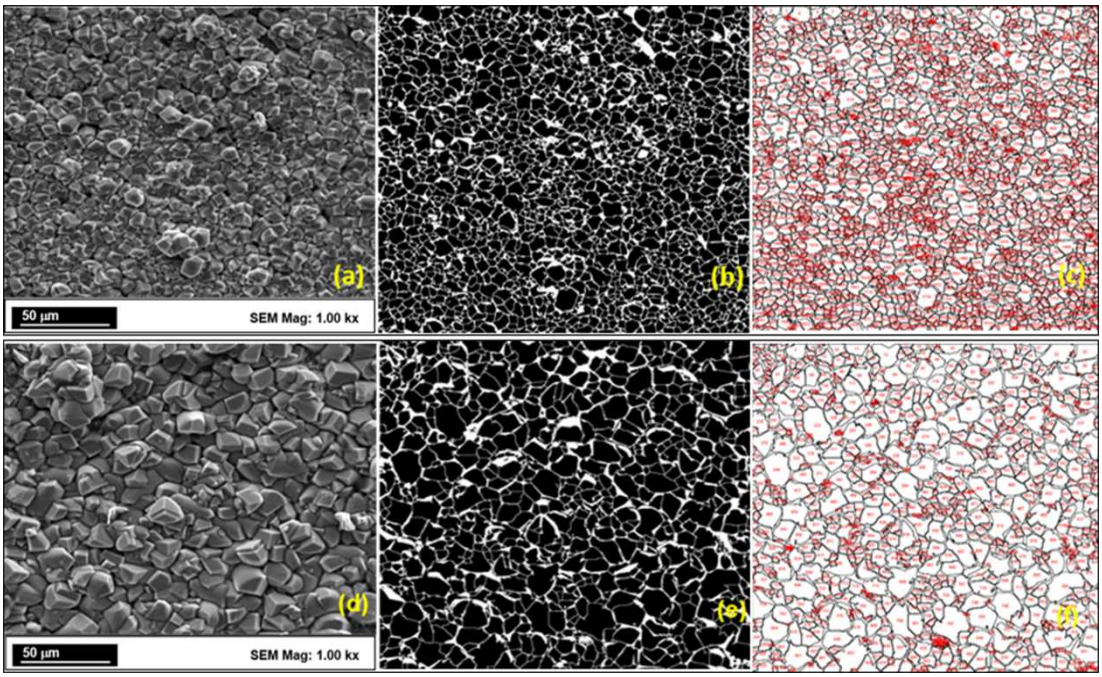

Figure 2: $FeCO_3$ film surface: (a) before hydrogen permeation test; (b) after image processing; (c) particles analysis and count. (d) after hydrogen permeation test; (e) after image processing; (f) analysis and count particles.

	Average particle size (μm)	%Area	Number of particles
Before permeation	16.41	76.33	1983
After permeation	35.12	79.84	968

Table 3: Average particle size, percentage of covered area by the film and number of particles of $FeCO_3$ on region observed, before and after hydrogen permeation test in CO_2-saturated 3.5 wt. % NaCl solution, under cathodic polarisation.

The barrier effect of the $FeCO_3$ film in the hydrogen permeation under cathodic polarisation can be explained by the transformation of the film during the test, as there was an increase in particle size. During the permeation test, for 1 h, after filling the cathodic side with 3.5 wt.% NaCl solution, the dissolution of the metal and the $FeCO_3$ film occurred while the OCP tended to stabilise. The dissolution of the metal and of the film generated Fe^{2+} ions, which remained in solution throughout the cathodic polarisation test. The dissolution process at OCP was followed by crystallization or precipitation on pre-existing crystals and crystal growth [22], during cathodic polarisation. Cathodic polarisation ensures that the corrosion of substrate can be minimised, in other words, hinders the dissolution of iron on the metal surface, preventing the additional precipitation of $FeCO_3$ by supersaturation. Nevertheless, on voids existing along the film, hydrogen generation occurs by the direct reduction of H^+ ions, together with the reduction of H_2CO_3 and of HCO_3^- ions generated by the presence of CO_2 in the environment. This reduction induces a local alkalinisation on these sites and favours the precipitation of $FeCO_3$ in the vicinity. Asher [7] determined the pH on an X65 steel surface immersed in CO_2-saturated $NaHCO_3$ solution, at different distances from the interface under cathodic polarisation. It was concluded that the pH became more alkaline on the steel surface, while in the bulk solution the pH was lower and constant. Moreover, there was not a continuous pH gradient along the distance from surface. Thus, when the specimen was at OCP and the pH on the surface kept acid, the $FeCO_3$ film dissolution, previously formed, was favoured, as it was also observed by Yang et al. [23]. Fe^{2+} ions arising from metal and $FeCO_3$ dissolution, diffuse to these alkaline microenvironments in the film voids, generating supersaturation and a new $FeCO_3$ precipitation. It was understood that morphology and particle size distribution observed are result of the modified nucleation and growth kinetics [24]. In other words, $FeCO_3$ crystal growth is due to the addition of more solute molecules to new nucleation sites or to the crystal lattice. Consequently, precipitated

crystals increase with defined shape and size [25]. At the molecular level, growth units diffuse to the crystal surface and then attach to the surface. These units can remain at their initial point of contact, diffuse across the surface and eventually integrate into the structure of the crystal or return to solution [24]. Thus, the pre-existing $FeCO_3$ crystals behave as a nucleus to the growth of the particles and a dynamic equilibrium between dissolution and growth occurs in this microenvironment, justifying the difference of particles sizes observed after hydrogen permeation under cathodic polarisation. This a phenomenon known as growth process of particles, by the dissolution of coexisting smaller particles, it is also called Ostwald ripening, in which the solubility of smaller particles is larger than this the larger ones, and mass transfer from smaller particles to larger occurs. In other words, pre-existing relatively large particles grow at the expense of a great amount of unstable small particles [26].

Ma et al [27] studied different conditions to conduct $FeCO_3$ precipitation experiments using EQCM (Electrochemical Quartz Crystal Microbalance), an actively corroding iron-coated quartz crystal and a cathodically polarised iron-coated quartz crystal, at varied temperatures (50-80 °C) were used in these tests. It was investigated how the nature of the substrate surface can affects the kinetics of $FeCO_3$ precipitation in an aqueous CO_2 environment. The results were compared with the Sun and Nesic model's calculation [28], which proposed the kinetic model to obtain the precipitation rate of $FeCO_3$ as a function of the solubility saturation index ($S_{FeCO3} = [Fe^{2+}]\ [CO_3^{2-}] / K_{sp,FeCO3}$) and temperature. Results of S_{FeCO3} were very close to those obtained for actively corroding and cathodically polarised iron-coated quartz crystals and results obtained for an actively corroding steel surface. Furthermore, precipitation rates obtained by S&N model calculation and experimental results of both surface conditions studied were also close in all temperatures, expressed by a linear relationship between precipitation rate and S_{FeCO3}. Furthermore, polarized iron-coated crystal surface presented larger particles compared to the actively corroding iron-coated crystal at 70°C. These results support the conclusion that it is possible to obtain higher $FeCO_3$ particles under cathodic polarisation.

Silva et al [11] performed hydrogen permeation tests under similar conditions, but with the steel interface kept at OCP. When compared the results with those presented on this work, lower hydrogen permeation currents were reached, on steady state, at OCP. However, in this work, carried out under cathodic polarisation, beyond higher permeation current values in each condition, the steady state was not observed in none of test conditions. It is also important to point out that the permeation current increased with time in wet-ground and Fe_3C surfaces, and dropped down for $FeCO_3$ surface when under cathodic polarisation.

Table 4 and Figure 3 show the parameters obtained from the hydrogen permeation curves under cathodic polarisation. The parameters are steady state hydrogen flux, effective hydrogen diffusivity, permeability and hydrogen concentration on the cathodic side of the sample, according to ASTM G148 [29]. The hydrogen concentration on the cathodic side and the steady state hydrogen flux are higher in the specimens with Fe_3C rich surface and lower in $FeCO_3$ film surface, as well as the permeability. However, the effective diffusivity is higher for the $FeCO_3$ film surface.

Parameters Test conditions	J_{ss} x 10^{-12} (mol/cm^2.s)	D_{eff} x 10^{-6} (cm^2/s)	P x 10^{-12} (mol/cm.s)	C_H x 10^{-6} (mol/cm^3)
Wet-ground_test 1	8.71	1.84	2.61	1.42
Wet-ground_test 2	8.82	2.00	2.64	1.33
Wet-ground_test 3	7.94	2.23	2.38	1.07
Fe_3C_test 1	10.12	1.81	3.03	1.67
Fe_3C_test 2	10.39	1.90	3.12	1.64
Fe_3C_test 3	9.63	1.96	2.89	1.47
$FeCO_3$_test 1	6.03	3.46	1.81	0.52
$FeCO_3$_test 2	6.31	5.36	1.89	0.36
$FeCO_3$_test 3	7.26	5.17	2.18	0.42

Table 4: Parameters obtained from hydrogen permeation curves in CO_2-saturated 3.5 wt.% NaCl solution under 500mV below OCP, according to ASTM G148 [29].

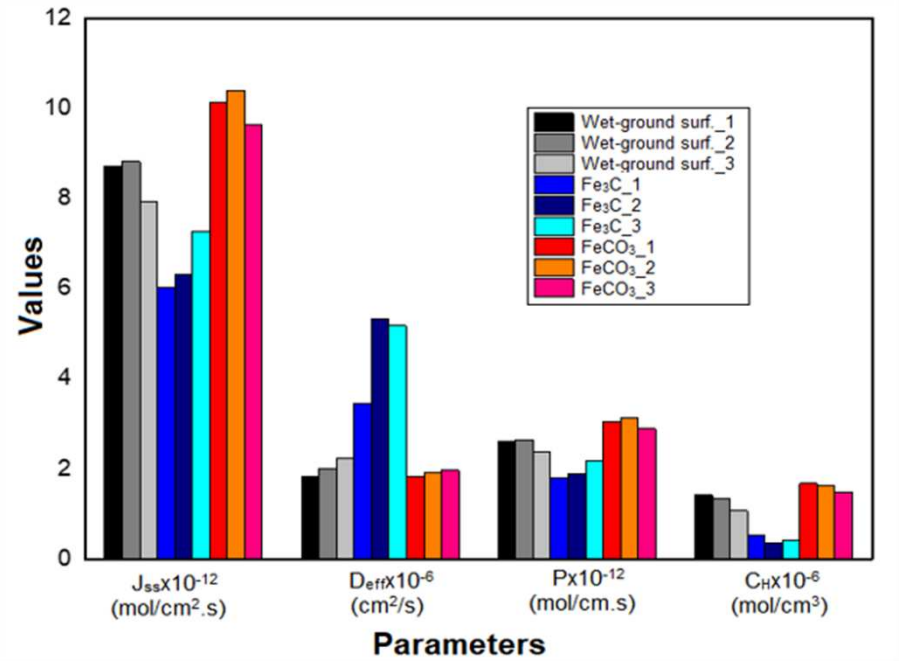

Figure 3: Parameters obtained from hydrogen permeation curves, in CO_2-saturated environment under 500mV below OCP, in wet-ground surface, Fe_3C-rich surface and $FeCO_3$-filmed surface according to ASTM G148 [29].

J_{ss} is the steady state hydrogen flow obtained from the Eq. (3).

$$J_{ss} = I_{ss} / (F. A) \quad \text{Eq. (3)}$$

Where, I_{ss} is the steady state permeation current, F is Faraday constant (96,485 C/mol) and A is the useful area of sample (1 cm^2).

D_{eff} is the effective hydrogen diffusivity gotten from the Eq. (4).

$$D_{eff} = L^2 / 6t_{lag} \quad \text{Eq. (4)}$$

Where, L is the thickness of sample and t_{lag} is the elapsed time to achieve 63% steady state flow.

P is the permeability obtained from the Eq. (5).

$$P = J_{ss} L \quad \text{Eq. (5)}$$

Finally, C_H is the surface hydrogen concentration on the cathodic side of the sample, obtained from Eq. (6).

$$C_H = J_{ss} L / D_{eff} \quad \text{Eq. (6)}$$

As the diffusion is a time dependent process, the hydrogen permeated amount is also function of time. This rate is expressed by the steady state hydrogen flow (J_{ss}). Steady state hydrogen flow was lower on $FeCO_3$ film surface, in which the hydrogen permeation current is high in the beginning of the test and tends to decrease with time due to the increase of particles size and also filled voids of the $FeCO_3$ film. Fe_3C-rich surface presented the highest steady state hydrogen flow, probably due to the increase of porosity of the pre-corroded surface, as confirmed by Mora-Mendoza and Turgoose [20] and Paolinelli et al [30]. These authors showed that films of corrosion products formed below 40°C in chloride environment containing CO_2 are porous. Meanwhile, on wet-ground surface an intermediate hydrogen flow was reached.

Effective hydrogen diffusivity (D_{eff}) is also known as the diffusion coefficient. This property qualifies the propagation velocity of hydrogen inside the metal, being the most important comparison parameter among metals. The calculated D_{eff} value is higher in $FeCO_3$ film surface than in Fe_3C rich and in wet-ground surface. This parameter is dependent on metal microstructure and the sample thickness. As Fe_3C and $FeCO_3$ enriched surfaces are biphasic specimens, it can be expected that hydrogen propagation velocity is different in each phase, which explains the difference of values among the three different surface compositions studied. Moreover, this fact can also explain the higher standard deviation of D_{eff} exhibited for the $FeCO_3$-filmed surface, Table 5.

Permeability (P) is the maximum amount of hydrogen that crosses a metal of known thickness. Permeability was also higher in Fe_3C rich surface. Hydrogen concentration (C_H) is related to the maximum concentration of absorbed hydrogen on the metal surface. Fe_3C rich surface presented higher hydrogen concentration.

Table 5 and Figure 4 present the average, standard deviation and variance of the steady state hydrogen flow, effective hydrogen diffusivity, permeability and surface hydrogen concentration on the cathodic side of samples from triplicate of hydrogen permeation tests. As indicated, all parameters present a low standard deviation, indicating that the data points tend to be close to the average, therefore confirming the repeatability of the tests.

	Average			**Standard Deviation**			**Variance**		
	Wet-ground surface	**Fe_3C**	**$FeCO_3$**	**Wet-ground surface**	**Fe_3C**	**$FeCO_3$**	**Wet-ground surface**	**Fe_3C**	**$FeCO_3$**
J_{ss} x 10^{-12} (mol/cm^2.s)	8.49	10.04	6.54	0.48	0.38	0.64	0.23	0.15	0.42
D_{eff} x 10^{-6} (cm^2/s)	2.02	1.89	4.65	0.19	0.073	1.03	0.038	0.0054	1.07
P x 10^{-12} (mol/cm.s)	2.55	3.01	1.96	0.14	0.115	0.19	0.021	0.013	0.037
C_H x 10^{-6} (mol/cm^3)	1.27	1.60	0.43	0.18	0.11	0.085	0.033	0.011	0.0071

Table 5: Statistical analysis of the steady state hydrogen flow, effective hydrogen diffusivity, permeability and surface hydrogen concentration on cathodic side of sample in a CO_2-saturated 3.5 wt.% NaCl solution under 500mV below OCP.

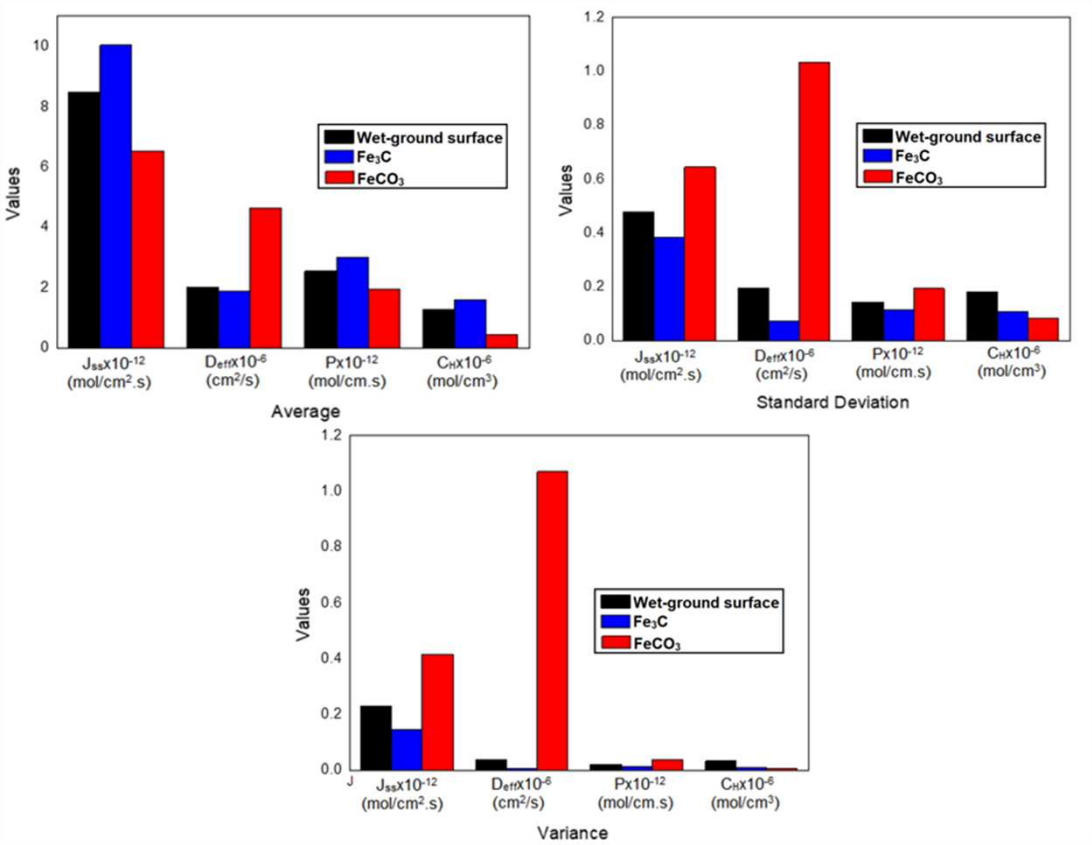

Figure 4: Statistical analysis of the steady state hydrogen flow, effective hydrogen diffusivity, permeability and surface hydrogen concentration on cathodic side of sample in CO_2-saturated 3.5 wt.% NaCl solution under 500mV below OCP.

3.3. Slow Strain Rate Tests

SSRTs were performed to assess the influence of hydrogen uptake in CO_2-saturated 3.5 wt.% NaCl solution on the mechanical resistance of the X65 steel at room temperature. Stress versus time curves and the parameters obtained from SSRT data in air and in CO_2-saturated solution are shown in Figure 5 and Table 6, respectively.

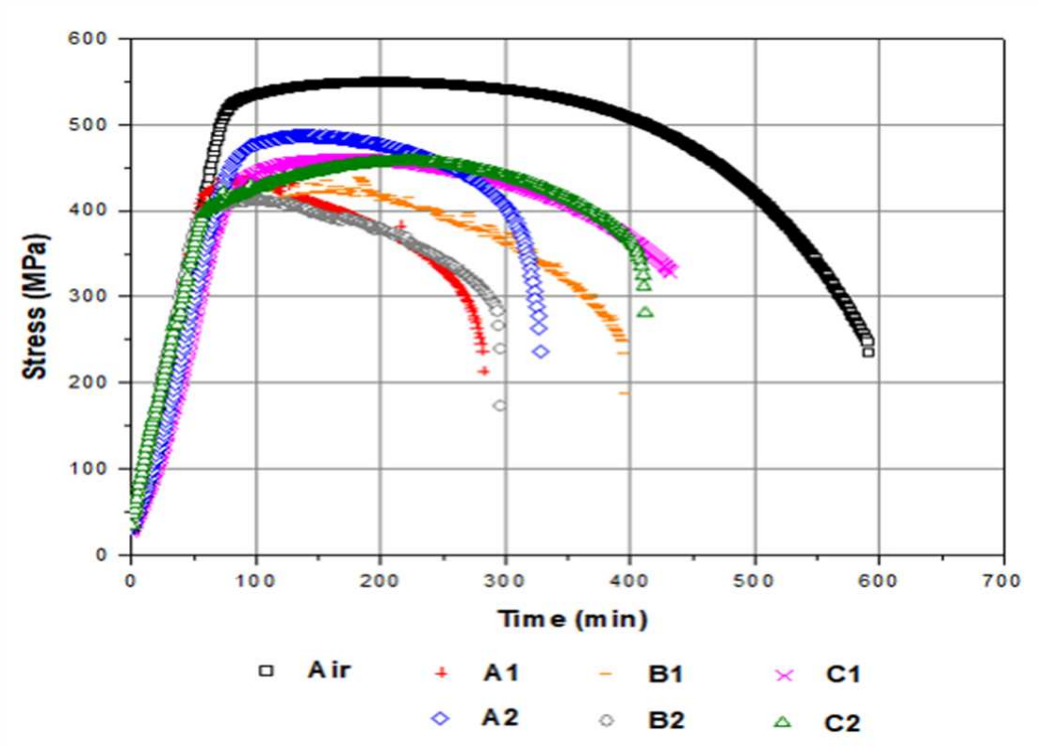

Figure 5: Stress versus time curves obtained from SSRTs at CO_2-saturated 3.5 wt.% NaCl solution, under cathodic potential of 500mV below OCP, in each surface condition. Air, A1 (wet-ground, t_0), A2 (wet-ground, t_1), B1 (Fe_3C, t_0), B2 (Fe_3C, t_1), C1 ($FeCO_3$, t_0), C2 ($FeCO_3$, t_1).

Table 6 shows the statistical analysis of average, standard deviation and variance of area reduction (RA) and time-to-failure (TTF) obtained from SSRT curves of conditions studied. The loss of ductility was evidenced by these parameters and also by the reduction of the elastic limit.

		Average		Standard Deviation		Variance	
		TTF (h)	RA% (SEM)	TTF (h)	RA% (SEM)	TTF (h)	RA% (SEM)
Air		9.68	87.083	0.16	1.809	0.026	3.271
Wet-ground surface	**A1**	4.86	37.404	0.40	1.413	0.16	1.997
	A2	5.92	52.573	0.59	2.822	0.35	7.965
Fe_3C	**B1**	6.62	51.356	0.18	2.377	0.031	5.648
	B2	5.12	53.902	0.32	1.779	0.10	3.165
$FeCO_3$	**C1**	6.89	39.344	0.37	1.567	0.14	2.456
	C2	6.92	56.300	0.11	2.847	0.012	8.106

Table 6: Statistical analysis of reduction in area (RA) and of time-to-failure (TTF) in CO_2-saturated 3.5 wt.% NaCl solution, under cathodic potential of 500 mV below OCP.

The first observation is that the steel has yield strength and tensile strength around 505 MPa and 536 MPa, respectively. Reduction in area and reduction of TTF were obtained from SEM analysis and stress versus time curves, respectively. The average of the time-to-failure (TTF) obtained in test in air was approximately 9 hours and 40 minutes, as shown in Table 6.

Table 6 also presents a lower RA in conditions A1 (wet-ground surface, t_0) and C1 ($FeCO_3$ surface, t_0) besides a more intense reduction of TTF in A1 (wet-ground surface, t_0) and B2 (Fe_3C surface, t_1) conditions.

Table 7 shows ratio of reduction in area (RRA) and ratio of time-to-failure (RTTF) for the X65 steel determined from the ratio between each test in corrosive environment and in the test in air, according to ASTM G129 standard [10].

		RTTF=(TTF_e/TTF_c)	RRA=(RA_e/RA_c)
Wet-ground surface	**A1**	0.502	0.429
	A2	0.612	0.604
Fe_3C	**B1**	0.684	0.590
	B2	0.529	0.619
$FeCO_3$	**C1**	0.712	0.452
	C2	0.715	0.647

Table 7: Ratios of reduction in area (RRA) and of time-to-failure (TTF) of X65 steel in CO_2-saturated 3.5 wt.% NaCl solution, under cathodic potential of 500 mV below OCP.

The loss of ductility of the material was also observed in the sample wet-ground in the CO_2-saturated environment with cathodic potential applied, since conditions A1 and A2 presented RRA values of 0.423 and 0.594, respectively (Table 7). The loss of mechanical property in the X65 steel in the A1 condition studied can be compared to similar carbon steels in H_2S environment. Ballesteros et al. [31] studied API 5L X80 steel in an H_2S environment and this presented an RRA of 0.472. This shows that the imposition of cathodic potential in the material, which means the intensification of the reduction of hydrogen, affects strongly the mechanical properties of the material, increasing embrittlement by hydrogen of the same. The same study carried out on steel X65, in surface conditions A1 and A2, at OCP, presented RRA values of 0.909 and 0.873,

respectively. The results in cathodic potential when compared to the results at OCP ratify that the imposition of cathodic potentials intensifies the hydrogen embrittlement of the steel [11].

It is important to observe that the OCP is higher in Fe_3C rich surface, indicating that the driving force for hydrogen reduction was lower, nevertheless, the hydrogen permeation is higher for this surface condition. Based on this hypothesis, hydrogen deleterious effects were observed in tests performed on the Fe_3C surface, B1 and B2 conditions. It was noted that a reduction of elastic limit in both conditions occurred, exhibiting the loss of ductility of the material. However, the hydrogen effect was more severe in B2 condition, both for the elastic limit as for the RTTF parameter value. This fact exhibits strong influence of the time of hydrogen permeation in embrittlement of the material. Under these conditions, the anodic dissolution process was extinguished due to the imposition of the cathodic potential and the intensification of the hydrogen reduction, increasing permeation and hydrogen embrittlement.

In the conditions C1 and C2 ($FeCO_3$ film surface), loss of ductility of the material occurred, since a smaller reduction in area was noticed, especially in condition C1, evidencing a higher embrittlement of the material. This can be explained by the fact that in the C1 condition the tensile load was applied at the instant in which the hydrogen permeation current is high, according to the curves obtained from permeation tests, under an imposed potential of -500mV_{OCP}. On the other hand, C2 condition, corresponding to the time required for the diffusion of the hydrogen in the steady state presented a less severe deleterious effect, which can be explained by the hydrogen permeation time. In this condition, an increase of $FeCO_3$ crystals was observed, forming a barrier to hydrogen permeation, making the embrittlement of the material less severe. However, the embrittlement observed in the material, according to reduction in area, is considered severe in both conditions, since the values of RRA of C1 and C2 were 0.445 and 0.637, respectively (Table 7). The effect of $FeCO_3$ film rupture should be also considered as an enhancer factor for the embrittlement of the material.

RRA presented in Table 7 ratifies the embrittlement of the X65 steel, under imposition of cathodic potential in all the studied conditions, showing the loss of ductility in the CO_2-saturated environment. These results when compared with those obtained by Bueno et al. [32], which showed that API 5L X60 steel exhibited loss of ductility due to hydrogen embrittlement in standard NS4 solution and modified standard NS4 under cathodic potential. However, the loss of ductility in X65 steel was lower than reported by Bueno et al [32], since the RRA obtained under cathodic polarisation was 0.287 in NS4 solution and 0.269 in NS4 containing H_2S.

3.4. Scanning Electron Microscopy Analysis (SEM)

Scanning Electron Microscope (SEM) analysis of fracture and lateral surfaces of SSRT specimens after testing is a basic requirement to achieve a better interpretation of the material behaviour in air and in the CO_2-saturated solution.

The conditions that presented higher embrittlement were A1 and B2 due to lower RRA and RTTF and C1 that also presented a low RRA. Fracture surfaces and final diameters of the steel after test in air, on wet-ground surface, A1 condition, and on $FeCO_3$ filmed surface, C1 condition are shown in Figure 6(a), (b) and (c), respectively. The sample of Figure 6(a), test in air, shows an elliptical shape and the diameter must be obtained by the measurement of both axes of the fracture surface. Likewise, the measurements were obtained for the other specimens, as shown in Figures 6(b) and (c), corresponding to the final diameters of most severe conditions observed for the material tested in CO_2 environment under cathodic potential.

It is noted that there was higher necking down for tests in air than in solutions, particularly in A1 and C1 conditions. It implies that the reduction in area, and consequently ductility, was lower in these conditions. These data comply with the data obtained from SSRT (Table 6), showing that the steel presented ductile fracture in air, with plastic deformation considerable, cup-and-cone morphology. However, in test A1 and C1 conditions there was a significant loss of ductility due to hydrogen embrittlement. Bueno et al. [32] also studied a ferrite-perlite microstructure steel, which also presented a similar ductile fracture surface, with great reduction in area in the SSRTs carried out in air, while in NS4 solution with bubbling of CO_2 presented to decrease of reduction in area, therefore the loss of mechanical properties. Bueno et al. [33] conducted another study in order to evaluate the stress corrosion cracking and hydrogen embrittlement in API grade steel. The behaviour of the steel in air, in soil and in NS4 standard solutions, under different potentials (OCP, -100 mV_{OCP}, -300 mV_{OCP}) was studied. The material studied presented a decreasing ductility as long as more cathodic potential was imposed and this effect was more evident in soil solution than in NS4 standard solution, besides that the cracking mechanism is related to the influence of hydrogen. Transgranular cracking occurred even under cathodic conditions where the anodic dissolution of the steel can be considered as negligible.

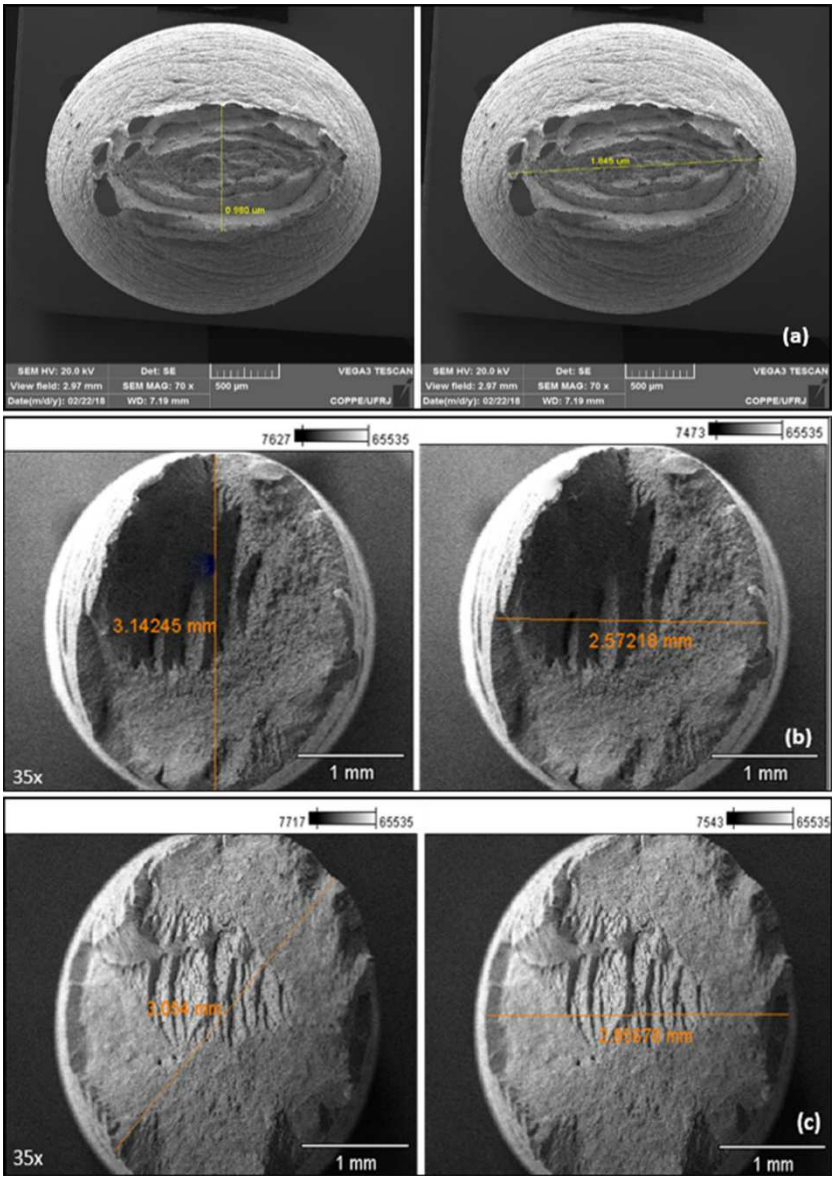

Figure 6: SEM: Fracture surfaces and measured diameters of the X65 steel after SSRTs in air and in CO_2-saturated environment. (a) Air. 70x. (b) Wet-ground, in CO_2-saturated environment, A1 condition. 35x. (c) $FeCO_3$ filmed surface, in CO_2-saturated environment condition C1. 33x.

Figure 7 shows the aspect of the lateral surface of steel after SSRT. Figures 7(a), (b) and (c) are related to the tests in air and in CO_2-saturated environment in conditions A1 and C1 under cathodic potentials, respectively. Figure 7(a) confirms the significant necking down of the material tested in air. The similar lateral surfaces of the specimens tested in A1 condition presents a reduced necking down and presence of secondary cracks, evidencing loss of ductility attributed to hydrogen embrittlement of the steel, since the anodic dissolution was suppressed, shown in Figure 7(b). Loss of ductility in condition

C1 was also confirmed, due to the similar reduced necking down, as noticed in Figure 7(c) and the presence of secondary micro-cracks on the lateral surface close to the necking down region. The presence of these micro-cracks implies that the fracture mechanism during SSRT is governed by the hydrogen effect. Hydrogen embrittlement usually manifest in carbon and low alloy steels with crack initiation and propagation characteristics [34]. The presence of surface films, such as $FeCO_3$, can drive to more critical embrittlement due to the rupture of the film, induced by the dynamic strain, forming preferential sites for entrance of hydrogen. In many cases of Environment Assisted Cracking the hydrogen effects are involved and interact with the localized crack-tip plasticity. Bueno et al [33] also noticed the presence of micro-cracks on lateral surface in X46 steel under different potentials (OCP, -100 mV_{OCP}, -300 mV_{OCP}), in soil and in NS4 standard solutions, showing that this cracking mechanism can be originated by hydrogen uptake and its interaction with the included material. Moreover, according to Vancostenoble et al. [35], although the precipitated $FeCO_3$ at the surface acts as a protective film reducing the corrosion rate, in presence of environmental fluctuations and/or stress and strain, this protective layer can be damaged, inducing fracture and leading to SCC or Hydrogen Embrittlement. Besides that, external cracking of pipelines is consequence of complex interactions between physical and chemical factors [36].

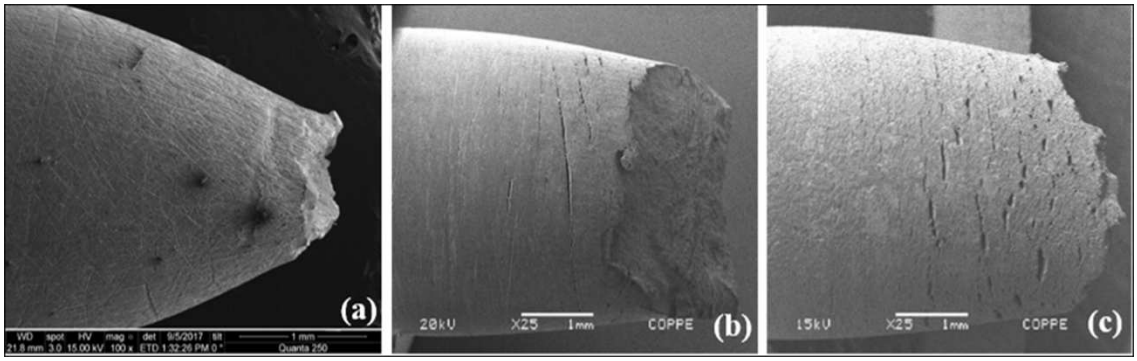

Figure 7: SEM: Lateral surfaces of the carbon steel after SSRTs in air and in CO_2-saturated environment. (a) Air. 100x. (b) Wet-ground surface, A1 condition. 25x. (c) $FeCO_3$ filmed surface, C1 condition. 25x.

Steel tested in air presented ductile fracture mechanism of cup-and-cone type, in which is observed the coalescing of micro-porosity, dimples, on the centre and on the edges of the fracture surface in Figures 8(a) and (b). This fracture surface presents the three characteristics of ductile fracture, which are: considerable plastic deformation in the region of ductile fracture; the applied shear stress exceeds the shear strength before

some other fracture modes can occur; and the appearance of the ductile fracture is matte and fibrous, that it is caused by the deformation at the fracture surface.

Figures 8(c) and (d) show fracture surface of carbon steel after test on wet-ground surface, in CO_2-saturated environment (A1 condition). Fracture surface exhibits a mixed appearance ductile and brittle, with very few and shallow dimples in the centre of the sample, evincing a ductile behaviour and with a part of the surface bright and faceted, ratifying a brittle behaviour. While on the surface edge, it is observed only a bright and faceted aspect. The fracture surface appearance in A1 condition exhibit the embrittlement of the material due to the hydrogen effects, ratifying the results presented in Table 7. This exposes a fracture process characterised by a transgranular cracking morphology, with the edges of the fracture surface presented brittle behaviour by cleavage, evidencing loss of ductility of the material.

In Figures 8(e) and (f) are observed images of sample after test on $FeCO_3$ film surface, C1 condition. Fracture surface presents few and shallow dimples on the middle and the edge of sample. Moreover, the edges of fracture surface also showed the brittle behaviour, with bright and faceted appearance. According to Fassina et al. [37] unstable crack propagation presents a typical aspect of transgranular cleavage, with secondary cracks transverse to the primary fracture. So, a mixed fracture morphology was observed, featuring both brittle fracture by cleavage and ductile fracture by dimples, confirming the hydrogen embrittlement of the steel.

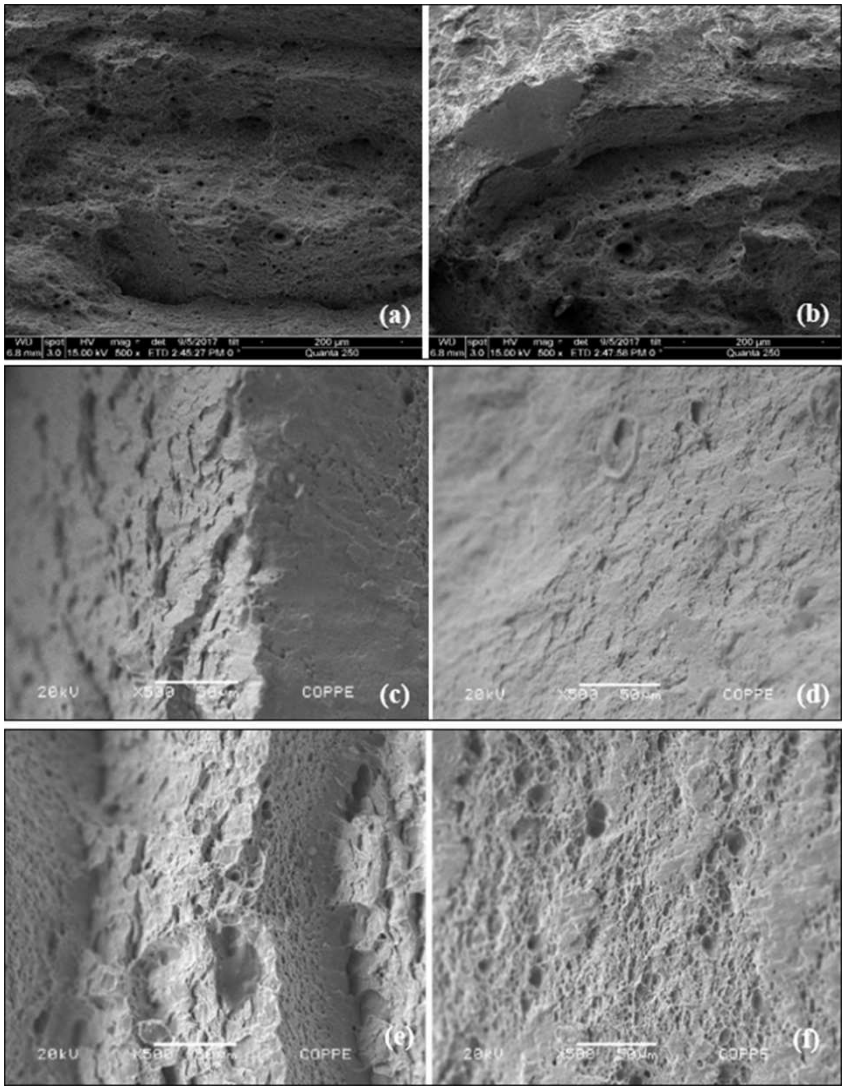

Figure 8: SEM: Fracture surfaces of the carbon steel after test in air and in A1, B2 and C1 conditions, respectively. Air: (a) Center; (b) Edge. Wet-ground surface, A1 condition: (c) Center; (d) Edge. $FeCO_3$ filmed surface, condition C1: (e) Center; (f) Edge. Magnification: 500x.

4. CONCLUSION

I. X65 steel is susceptible to environment assisted cracking in pure CO_2 solution under cathodic polarisation, a condition in which the hydrogen reduction reaction is intensified. The loss of ductility is driven by hydrogen that permeates in API 5L X65 steel. This conclusion is supported by the results obtained from Slow Strain Rate Tests and Hydrogen Permeation tests. Moreover, the data obtained suggest a similar critical detrimental effect than the one observed for the same material in H_2S environments.

II. The magnitude of the embrittlement effect depends on the steel surface composition. The hydrogen permeation current density tends to increase with the time into the wet-ground surface under cathodic potential. However, the presence of Fe_3C increases the hydrogen permeation in the steel, exhibiting higher values of permeation current density since it accentuates the cathodic reaction in the diffusion limit region, so that the hydrogen reduction reaction is facilitated in this condition surface, enhancing the hydrogen permeation into the steel.

III. The permeation current into the $FeCO_3$ filmed steel surface reaches a higher value at the beginning of the test and tends to decrease over time. It can occur because there were some voids within the film when the cathodic potential was applied, the crystal size of $FeCO_3$ tends to increase, forming a thicker film, and thus a barrier to the hydrogen permeation. This fact can be explained by the aging of precipitated later.

IV. Parameters obtained from SSRT, such as RA and TTF decreased at every CO_2 environment test condition. The elastic limit reduction was also registered as an indication of detrimental effect of the CO_2 environment, assisted by secondary micro-cracks on the wet-ground surface, A1 condition, and on $FeCO_3$ film surface, C1 condition.

ACKNOLEDGEMENT

The authors would like to acknowledge the support provided by CNPq and Shell.

REFERENCES

[1] Dugstad, A. (1992). The Importance of $FeCO_3$ Supersaturation on the CO_2 Corrosion of Carbon Steels, NACE International, Houston, TX, March 1992, Paper 14.

[2] Dong, C. F., Xiao, K., Liu, ZY., Yang, WJ., Li, XG. (2010). Hydrogen induced cracking of X80 pipeline steel. International Journal of Minerals, Metallurgy and Materials. 17 (5), 579–586. DOI: 10.1007/s12613-010-0360-2

[3] Liang, P., Du, CW., Li. XG., Chen, X. Zhang, L. (2009). Effect of hydrogen on the stress corrosion cracking behavior of X80 pipeline steel in Ku'erle soil simulated solution. International Journal of Minerals, Metallurgy and Materials. 16 (4), 407-413. DOI: 10.1016/S1674-4799(09)60072-8

[4] Huang, F., Li, X.G., Liu, J., Qu, Y.M., Ji, J. and Du, C.W. (2011). Hydrogen-induced cracking susceptibility and hydrogen trapping efficiency of different microstructure X80

pipeline steels. Journal of Materials Science. 46. 715-722. DOI: 10.1007/s10853-010-4799-3

[5] Kermani, M.B. and Morshed, A. (2003). Carbon Dioxide Corrosion in Oil and Gas Production - A Compendium. Corrosion. 59 (8), 659-683. DOI: 10.5006/1.3277596

[6] Dugstad, A., Lunde, L. and Nesic, S. (1994). Control of internal corrosion in multi-phase oil and gas pipelines. Prevention of Pipeline Corrosion Conference. Pipe Line Industry and Pipes & Pipelines International, Houston, Texas, USA.

[7] Asher, S. L. (2007). Investigating the mechanism of transgranular stress corrosion cracking in near-neutral pH environments on buried fuel transmission pipelines. A Dissertation presented to The Academic Faculty. Doctor of Philosophy in the School of Materials Science and Engineering. Georgia Institute of Technology. 120, 171-175.

[8] Rogowska, M., Gudme, J., Rubin, A., Pantleon, K. and Ambat, R. (2016). Effect of Fe ion concentration on corrosion of carbon steel in CO_2 environment. Corrosion Engineering, Science and Technology. 51(1), p.25-36. DOI: 10.1179/1743278215Y.0000000029

[9] NACE Standard TM0198 (2016). Slow strain rate test method for screening corrosion-resistant alloys for stress corrosion cracking in sour oilfield service. ISBN: 1-57590051-3

[10] ASTM G129–95 (2000). Slow Strain Rate Testing to Evaluate the Susceptibility of Metallic Materials to Environmentally Assisted Cracking. DOI: 10.1520/G0129-00

[11] Da Silva, S. C., de Souza, E. A., Pessu, F., Hua, Y., Barker, R., Neville, A., Ponciano Gomes, J. A. C. (2019). Cracking mechanism in API 5L X65 steel in a CO_2-saturated environment. Engineering Failure Analysis. 99, 273-291. DOI: 10.1016/j.engfailanal.2019.02.031

[12] Farelas, F., Galicia, M., Brown, B., Nesic, S. and Castaneda, H. (2010). Evolution of dissolution processes at the interface of carbon steel corroding in a CO_2 environment studied by EIS. Corrosion Science. 52 (2), 509-517. DOI: 10.1016/j.corsci.2009.10.007

[13] Nesic, S., Thevenot, N., Crolet, J. L. and Drazic, D. M. (1996). Electrochemical properties of iron dissolution in the presence of CO_2 - Basics revisited. NACE Corrosion Conference 1996, Houston, TX (United States). Proceedings of NACE Corrosion 1996. Paper n° 3. ISBN: 96003 1996 CP

[14] Crolet, J.L., Thevenot, N. and Nesic, S. (1998). Role of Conductive Corrosion Products in the Protectiveness of Corrosion Layers. Corrosion. 54 (3), 194-203. DOI: 10.5006/1.3284844

[15] Hua, Y., Barker, R., Charpentier, T., Ward, M. and Neville, A. (2015). Relating iron carbonate morphology to corrosion characteristics for water-saturated supercritical CO_2 systems. The Journal of Supercritical Fluids. 98, 183-193. DOI: 10.1016/j.supflu.2014.12.009

[16] Dugstad, A., Hemmer, H. and Seiersten, M. (2001). Effect of steel microstructure upon corrosion rate and protective iron carbonate film formation. Corrosion. 57(4), 369-378. DOI: 10.5006/1.3290361

[17] Remita, E., Tribollet, B., Sutter, E., Vivier, V., Ropital, F., and Kittel, J. (2008). Hydrogen evolution in aqueous solutions containing dissolved CO_2: quantitative contribution of the buffering effect. Corrosion Science, 50 (5), 1433-1440. DOI: 10.1016/j.corsci.2007.12.007

[18] Beverskov, B., Puigdomenech, I. (1996). Revised Pourbaix Diagrams for iron at 25-300°C. Corrosion Science. 38 (12), 2121-2135. DOI: 10.1016/S0010-938X(96)00067-4

[19] Pourbaix, M. Atlas of Electrochemical Equilibria in Aqueous Solution, 1st ed.; Pergamon Press: Bristol, UK, 1966.

[20] Mora-Mendoza, J. L.; Turgoose, S. (2002). Fe_3C influence on the corrosion rate of mild steel in aqueous CO_2 systems under turbulent flow conditions. Corrosion Science. 44. p.1223-1246. DOI: 10.1016/S0010-938X(01)00141-X

[21] Barker, R., Hua, Y. and Neville, A. (2017). Internal corrosion of carbon steel pipelines for dense-phase CO_2 transport in carbon capture and storage (CCS) – a review. International Materials Reviews. 62 (1), 1-31. DOI: 10.1080/09506608.2016.1176306

[22] El-Zhry El-Yafi, A. K., El-Zein, H. (2015). Technical crystallization for application in pharmaceutical material engineering: Review article. Asian Journal of pharmaceutical sciences. 10 (4), 283-291. DOI: 10.1016/j.ajps.2015.03.003

[23] Yang, Y., Brown, B., Nesic, S. (2013). Study of protective iron carbonate layer dissolution in a CO_2 corrosion environment. NACE Corrosion Conference 2013. Paper n° 2708. ISBN: 02708 2013 CP

[24] Dirsken, J.A., Ring, T.A. (1991). Fundamental of crystallization: Kinetic effects on particle size distributions and morphology. Chemical Engineering Science. 46 (10), 2389-2427. DOI: 10.1016/0009-2509(91)80035-W

[25] Buckton G. (2007). Solid-state properties, Aulton's pharmaceutics. The science of dosage form design, Aulton M.E. 3rd ed. London: Churchill Livingstone. p. 110-120.

[26] Liu, X.J., Wang, H., Su, C. H., Zhang, P. W., Bai, J. B. (2010). Controlled fabrication and characterization of microspherical $FeCO_3$ and α-Fe_2O_3. Journal of Colloid Interface Science. 351(2), 427–432. DOI: 10.1016/j.jcis.2010.08.017

[27] Ma, Z., Yang, Y., Brown, B., Nesic, S. and Singer, M. (2018). Investigation of precipitation kinetics of $FeCO_3$ by EQCM. Corrosion Science. 141, 195-202. DOI: 10.1016/j.corsci.2018.06.017

[28] Sun, W., Nesic, S. (2008). Kinetics of corrosion layer formation: Part 1 – Iron carbonate layers in carbon dioxide corrosion. Corrosion. 64 (4), 334–346. DOI: 10.5006/1.3278477

[29] ASTM G148-97 (2011). Evaluation of hydrogen uptake, permeation and transport in metals by an electrochemical technique. DOI: 10.1520/G0148-97R11

[30] Paolinelli, L. D., Pérez, T., Simison, S. N. (2008). The effect of pre-corrosion and steel microstructure on inhibitor performance in CO_2 corrosion. Corrosion Science. 50 (9), 2456-2464. DOI: 10.1016/j.corsci.2008.06.031.

[31] Ballesteros, A.F., Gomes, J.A.C.P. and Bott, I.S. (2010). Study of the susceptibility of API 5L X80 girth welds to sulphide stress corrosion cracking and hydrogen embrittlement. Proceedings of the 8th International Pipeline Conference. Vol. 1. IPC2010-31243. DOI: 10.1115/IPC2010-31243

[32] Bueno, A.H.S., Moreira, E.D., Siqueira, P. and Gomes, J.A.C.P. (2014). Effect of cathodic potential on hydrogen permeation of API grade steels in modified NS4 solution. Materials Science & Engineering A. 597. p.117-121. DOI: 10.1016/j.msea.2013.12.033

[33] Bueno, A.H.S., Moreira, E.D., Gomes, J.A.C.P. (2014). Evaluation of stress corrosion cracking and hydrogen embrittlement in an API grade steel. Engineering Failure Analysis. 36, 423-431. DOI: 10.1016/j.engfailanal.2013.11.012

[34] Ghosh, G., Rostron, P., Garg, R., Panday, A. (2018) Hydrogen induced cracking of pipeline and pressure vessel steels: A review. Engineering Fracture Mechanics. 199, 609-618. DOI: 10.1016/j.engfracmech.2018.06.018

[35] Vancostanable, A., Duret-Thual, C., Bosh, C., Delafosse, D. (2014). Stress Corrosion Cracking of ferrito-pearlitic steel in aqueous environment containing dissolved CO_2. NACE Corrosion Conference 2014, Houston, TX (United States). NACE International. ISBN 4321 2014 CP, 2014.

[36] Mohtadi-Bonab, M.A., Szpunar, J.A., Razavi-Tousi S.S. (2013). A comparative study of hydrogen induced cracking behavior in API 5L X60 and X70 pipeline steels. Engineering Failure Analysis. 33, 163-175. DOI: 10.1016/j.engfailanal.2013.04.028

[37] Fassina, P., Bolzoni, F.,Fumagalli, G.,Lazzari, L., Vergani, L., Sciuccati, A. (2012). Influence of hydrogen and low temperature on mechanical behaviour of two pipeline steels. Engineering Fracture Mechanics. 81, 43-55. DOI: 10.1016/j.engfracmech.2011.09.016